Particle motion in unsteady two-dimensional peristaltic flow with application to the ureter

Joel Jiménez-Lozano, Mihir Sen, and Patrick F. Dunn
Department of Aerospace and Mechanical Engineering, University of Notre Dame, Notre Dame, Indiana, 46556 USA
(Received 11 December 2008; revised manuscript received 6 February 2009; published 1 April 2009)

Particle motion in an unsteady peristaltic fluid flow is analyzed. The fluid is incompressible and Newtonian in a two-dimensional planar geometry. A perturbation method based on a small ratio of wave height to wavelength is used to obtain a closed-form solution for the fluid velocity field. This analytical solution is used in conjunction with an equation of motion for a small rigid sphere in nonuniform flow taking Stokes drag, virtual mass, Faxén, Basset, and gravity forces into account. Fluid streamlines and velocity profiles are calculated. Theoretical values for pumping rates are compared with available experimental data. An application to ureteral peristaltic flow is considered since fluid flow in the ureter is sometimes accompanied by particles such as stones or bacteriuria. Particle trajectories for parameters that correspond to calcium oxalates for calculosis and *Escherichia coli* type for bacteria are analyzed. The findings show that retrograde or reflux motion of the particles is possible and bacterial transport can occur in the upper urinary tract when there is a partial occlusion of the wave. Dilute particle mixing is also investigated, and it is found that some of the particles participate in the formation of a recirculating bolus, and some of them are delayed in transit and eventually reach the walls. This can explain the failure of clearing residuals from the upper urinary tract calculi after successful extracorporeal shock wave lithotripsy. The results may also be relevant to the transport of other physiological fluids and industrial applications in which peristaltic pumping is used.

DOI: 10.1103/PhysRevE.79.041901 PACS number(s): 87.85.gf, 47.63.mf, 47.55.Kf

I. INTRODUCTION

Peristalsis is a mechanism of fluid transport in which a progressive wave of area contraction or expansion propagates along the length of the wall of a distensible tube or channel that contains fluid. The literature on peristaltic flow is now quite extensive [1–11]. Early analyses of peristaltic motion were simplified by introducing approximations such as periodic sinusoidal wave trains in infinitely long tubes or channels, small wall slopes, or low flow Reynolds number. The main objectives were to characterize the basic fluid mechanics of the process and, in particular, to find the pressure gradients that are generated by the wave, the flow behavior in the tube or channel due to peristalsis, and the conditions for trapping or reflux. Peristaltic pumps were developed and are currently used for industrial and medical applications. One of their main advantages lies in their ability to transport corrosive or very pure materials so as to prevent direct contact of the fluid with the pump's internal surfaces.

Numerical methods have been employed to model peristalsis of a single-phase fluid in a circular cylindrical tube at low Reynolds number and small slopes at the wall using finite differences [8], finite volumes [9], and in two-dimensional channels using a boundary integral method for Stokes flow [12]. Experimental studies of peristaltic flow include those by Yin and Fung [10], who studied a planar two-dimensional geometry and compared their results with an analytical solution, and the work of Weinberg *et al.* [13] for planar flow which includes flow visualization. Graw and Engelhardt [14] set up an experimental facility to emulate ureteral peristalsis, and the influence of thickness and luminal position of the catheter on pressure measurements during peristaltic activity was investigated. Peristaltic fluid flow can be accompanied by solid particles. Hung and Brown [15] studied experimentally the motion of large solid particles with particle diameter/wavelength $=\{0.021;0.103;0.186;0.259\}$ in a two-dimensional peristaltic flow.

Calculation of the motion of small particles in a fluid flow is of fundamental importance in many applications, for example, hydrosols, cells and particles in blood, microorganisms in a solution, and hydraulic transport of particles, among others. Solution methods for this type of problems depend on the parameter-range criteria [16]. The Stokes number characterizes the behavior of particles suspended in a fluid flow, $\mathrm{St}=\tau_v/\tau_f$, where τ_v is the particle relaxation time and τ_f is some time characteristic of the flow field. For a flow mixture $\mathrm{St}\approx 0$, and the problem can be solved with single-phase flow models using modified fluid properties or two-phase flow models (which is appropriate if the dispersed particle phase behaves like a continuum), such as non-Newtonian models or separated formulations for mass and momentum conservation for each phase. In particle suspension flows in which $0<\mathrm{St}<1$, trajectory models can be used with one-way coupling in a dilute suspension in which the fluid is treated as Eulerian and the particle motion as Lagrangian. In flows with two interacting components (gas-solid, gas-liquid, liquid-solid, liquid-gas, liquid-liquid), if $\mathrm{St}<1$, a two-way coupling can be included using a point-volume formulation with additional collision and interaction forces (Eulerian-Lagrangian), interpenetrating phases (Eulerian-Eulerian), or direct simulation methods. Most studies are conducted numerically, where the particle equation of motion is either solved through iterative schemes, or is simplified to allow for fast computations. Patankar and Joseph [17] used this formulation where each computational parcel is considered to represent a group of particles interacting with the fluid and possessing the same characteristics of size and composition. The positions of these parcels are then calculated using Newton's second law. Two-phase flow models are studied in [16,18–20] with applications to peristalsis in [21–24].

For the motion of a small spherical particle suspended in a fluid, a well-known model is the Basset-Boussinesq-Oseen (BBO) equation. This equation is applicable for small par-

ticles with Stokes drag, but modifications have been made to include other types of forces. Maxey and Riley [25] studied the particle motion under nonuniform flow and analytically derived an equation of particle motion in which many forces are considered. The effects of spatial variations in undisturbed and disturbed flows were taken into account. A general solution of the particle equation of motion in unsteady Stokes flows was presented by Coimbra and Rangel [26].

In this paper the BBO equation will be employed to analyze particle motion in peristaltic fluid flow. Peristaltic flow is of particular importance since it is present in nature. In biological systems, it is known that peristalsis is used to transport material and fluids. For example, physiological fluids in human or animals are, in general, propelled by the continuous periodic muscular contraction or expansion (or both) of the ducts through which the fluids pass. In particular, peristaltic mechanisms may be involved in the swallowing of food through the esophagus, vasomotion of small blood vessels, spermatic flows in the ductus efferentes of the male reproductive tract, embryo transport in the uterus, and transport of urine through the ureters, among others [27].

The urinary system is responsible for the homeostatic regulation of water and ion content of blood and the disposal of waste products of metabolism. The kidneys receive blood from the renal artery, process it, and return the processed blood to the body through the renal vein. Urine produced in the kidneys passes to the ureters. Under normal conditions, peristalsis in the upper urinary tract begins with the origin of electrical activity at pacemaker sites located in the proximal portion of the urinary collecting system. This electrical activity propagates distally, causing the mechanical event of peristalsis and renal pelvic and ureteral contractions, which propel the urine from the kidney to the bladder [28]. Urine is expelled through the urethra to the outside of the body. Lykoudis and Roos [6] studied the ureter fluid flow under a lubrication approximation and focused their analysis on the pressure profile in the contracted part. Griffiths [7] studied the ureter with a one-dimensional lubrication approach and emphasized the relation between low and high flow rates, pressure fields, and peristaltic contractions. Peristaltic flow in the ureter presents itself as an important application of peristalsis; the parameters are reasonably well known, and fluid being transported is essentially Newtonian and incompressible. Geometrically, however, the problem is complex. Peristaltic waves in the ureter can occur in many forms, either isolated or periodical, with complete occlusion during a cycle. Though the ureter is itself a tubular conduit, the lumen configuration during peristalsis could change since its inner layer is composed of a mucosa lined with a transitional epithelium. For simplicity, the configuration here is taken to be planar, which has previously been shown to exhibit similar peristaltic features as axisymmetry [1]. Also, experimental data are available for two-dimensional peristaltic flow [13] for verification. The main aim, in any case, is to get some physical insights into situations that may occur, such as retrograde flow and retrograde particle migration.

In the present study, the geometrical form of the peristaltic wave will be taken to be sinusoidal. The governing equations are Navier-Stokes for the fluid and momentum for the particle (BBO equation). A regular perturbation series in

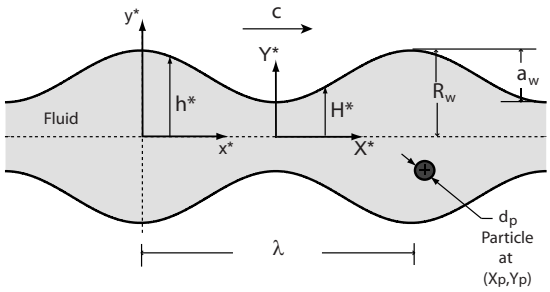

FIG. 1. Geometry of the sinusoidal periodic wave and an immersed particle in the medium.

which the variables are expanded in a power series of the wave number ϵ is used to solve the fluid problem. Closed-form solutions of the Eulerian velocity field up to order ϵ^2 are presented, and the range of validity of the approximation is investigated. The analytical solution has the advantage in that the Lagrangian particle paths can be determined by numerical solution of the ordinary differential equations of the trajectory. This could not be done if the fluid velocity field were to be calculated numerically (by finite differences, for example) because then the vector field would only be known at discrete points. One-way coupling between the fluid and particles is assumed, implying that fluid motion affects particle motion and not vice versa. This situation occurs in dilute suspensions when the interparticle spacing is more than about 100 times the particle diameter d_p, which is true for the cases examined in this study. An application to ureteral peristaltic flow is made. Particle trajectories for different parameters are investigated, and the mixing of a dilute group of particles is presented.

II. FORMULATION OF THE FLUID PROBLEM AND SOLUTION

Consider peristaltic flow of an incompressible Newtonian fluid in a two-dimensional channel with flexible walls. An infinite train of sinusoidal waves is assumed to move with constant velocity along the walls in the X^* direction. The wall itself, however, moves in a purely transverse direction. In Cartesian coordinates (X^*, Y^*), shown in Fig. 1, the channel walls are given by

$$H^*(X^* - ct^*) = R_w - a_w\{1 - \cos^2[\pi(X^* - ct^*)/\lambda]\},$$

where R_w is total wave height, a_w is the wave amplitude, λ is the wavelength, and c is the wave speed. The equations of motion for an incompressible Newtonian fluid in dimensional form are

$$\breve{\nabla}^* \cdot \bar{U}_f^* = 0,$$

$$\rho\left(\frac{\partial \bar{U}_f^*}{\partial t^*} + \bar{U}_f^* \cdot \breve{\nabla}^* \bar{U}_f^*\right) = -\breve{\nabla}^* P^* + \mu \breve{\nabla}^{*2} \bar{U}_f^*,$$

where ρ is the fluid density, μ is the fluid viscosity, t^* is the time, P^* is the pressure, and $\bar{U}_f^* = \{U^*, V^*\}$ are the axial and transverse velocities, respectively. The operator $\breve{\nabla}^* = \mathbf{i}\partial/\partial X^* + \mathbf{j}\partial/\partial Y^*$.

In the fixed frame (X^*, Y^*) the flow is unsteady. However, if we choose a frame of reference (x^*, y^*) that moves with velocity c in the X^* direction, the flow can be treated as steady. The transformation from a fixed to the moving frame in coordinates is $x^* = X^* - ct^*$, $y^* = Y^*$, and in the velocity components are $u^* = U^* - c$ and $v^* = V^*$. For the pressure $p^*(x^*, y^*) = P^*(X^*, Y^*, t^*)$. The dimensional equation of the wall at the moving frame is

$$h^*(x^*) = R_w - a_w\{1 - \cos^2[\pi(x^*)/\lambda]\}.$$

The dimensional form of the governing equations for the planar problem in the moving frame of reference is given by

$$\frac{\partial u^*}{\partial x^*} + \frac{\partial v^*}{\partial y^*} = 0,$$

$$v^*\frac{\partial v^*}{\partial y^*} + u^*\frac{\partial v^*}{\partial x^*} = -\frac{1}{\rho}\frac{\partial p^*}{\partial y^*} + \nu\left[\frac{\partial^2 v^*}{\partial y^{*2}} + \frac{\partial^2 v^*}{\partial x^{*2}}\right],$$

$$v^*\frac{\partial u^*}{\partial y^*} + u^*\frac{\partial u^*}{\partial x^*} = -\frac{1}{\rho}\frac{\partial p^*}{\partial x^*} + \nu\left[\frac{\partial^2 u^*}{\partial y^{*2}} + \frac{\partial^2 u^*}{\partial x^{*2}}\right],$$

where $\nu = \mu/\rho$ is the fluid kinematic viscosity, p^* is the pressure, and u^* and v^* are the axial and transverse velocities, respectively.

Dimensionless quantities are defined as $x \equiv \pi x^*/\lambda$ and $y \equiv y^*/R_w$ for the spatial coordinates. For the velocities $u \equiv u^*/c$ and $v \equiv v^*/\epsilon c$, and for the pressure $p \equiv \epsilon R_w p^*/\mu c$. Two geometrical dimensionless parameters present themselves in this formulation, the amplitude ratio $\phi \equiv a_w/R_w$ and the wave number $\epsilon \equiv \pi R_w/\lambda$. The Reynolds number is defined as $\mathrm{Re} \equiv R_w c/\nu$. By introducing the dimensionless stream function ψ (where $u = \partial\psi/\partial y$ and $v = -\partial\psi/\partial x$), which automatically satisfies the continuity equation, and eliminating the pressure from the Navier-Stokes equations by cross differentiation, the governing equations are reduced to

$$\epsilon\mathrm{Re}[\psi_y\nabla^2\psi_x - \psi_x\nabla^2\psi_y] = \nabla^2(\nabla^2\psi), \tag{1}$$

where the partial derivatives are denoted by subscripts. The modified Laplacian is given by $\nabla^2 \equiv \epsilon^2\partial^2/\partial x^2 + \partial^2/\partial y^2$. This is a stream-function formulation of the flow equations.

The dimensionless equation of the wall in the fixed frame is $H(X-t) = 1 - \phi\{1 - \cos^2(X-t)\}$, where $t \equiv c\pi t^*/\lambda$, $X \equiv \pi X^*/\lambda$, and $Y \equiv Y^*/R_w$. In the moving frame it is $h(x) = 1 - \phi\{1 - \cos^2(x)\}$.

The dimensional instantaneous flow rate in the fixed frame is given by

$$Q^* = \int_{-H^*}^{H^*} U^* dY^* = 2\int_0^{H^*} U^* dY^*. \tag{2}$$

Using the transformation between frames for coordinates and velocities, and by integration of Eq. (2), $Q^* = 2\int_0^{h^*} u^* dy^* + 2ch^*$ is obtained. The dimensional time–mean flow over a period T_w at a fixed X position is defined as

$$\hat{Q} \equiv \frac{1}{T_w}\int_0^{T_w} Q^* dt^*. \tag{3}$$

Substituting Q^* into Eq. (3) and using the dimensionless flow rates $q \equiv q^*/2cR_w$ and $Q \equiv \hat{Q}/2cR_w$, it is found that

$$Q = q + \left(1 - \frac{\phi}{2}\right), \tag{4}$$

where q is flow rate in the moving coordinate system and is independent of time. The boundary conditions for this problem are the no-slip condition at the wall and symmetry conditions along the centerline of the channel. If we choose the zero value of the streamline at the centerline $(y=0)$, $\psi=0$, then the wall $(y=h)$ is a streamline of value $\psi=q$ [1,11,23,29]. The dimensionless boundary conditions in the moving frame are

$$\frac{\partial^2\psi}{\partial^2 y} = 0, \quad \psi = 0 \quad \text{at } y = 0, \tag{5a}$$

$$\frac{\partial\psi}{\partial y} = -1, \quad \psi = q \quad \text{at } y = h(x). \tag{5b}$$

The independent variables in physical space (x, y) can be changed to a new set in a transformed space (Σ, Υ), where

$$\Sigma = x, \tag{6a}$$

$$\Upsilon = \frac{y}{h(x)}. \tag{6b}$$

This produces a domain transformation of the channel with sinusoidal walls to one with straight walls, and simplifies the solution of the problem when dealing with the boundary conditions. The channel walls are now located at $\Upsilon = \pm 1$. The governing equation [Eq. (1)] in this new domain is

$$\epsilon\mathrm{Re}[D_\Upsilon\psi\tilde{\nabla}^2 D_\Sigma\psi - D_\Sigma\psi\tilde{\nabla}^2 D_\Upsilon\psi] = \tilde{\nabla}^2(\tilde{\nabla}^2\psi), \tag{7}$$

where $D_\Sigma = \partial/\partial\Sigma - \Upsilon(h'/h)\partial/\partial\Upsilon$, $D_\Upsilon = (1/h)\partial/\partial\Upsilon$, and

$$\tilde{\nabla}^2 \equiv \epsilon^2\left\{\frac{\partial^2}{\partial\Sigma^2} + \Upsilon^2\left(\frac{h'}{h}\right)^2\frac{\partial^2}{\partial\Upsilon^2} - 2\Upsilon\left(\frac{h'}{h}\right)\frac{\partial}{\partial\Sigma\,\partial\Upsilon} + \left[2\Upsilon\left(\frac{h'}{h}\right)^2 - \Upsilon\left(\frac{h''}{h}\right)\right]\frac{\partial}{\partial\Upsilon}\right\} + \frac{1}{h^2}\frac{\partial^2}{\partial\Upsilon^2}.$$

The corresponding boundary conditions [Eq. (5)] in the transformed system are

$$\frac{\partial^2\psi}{\partial^2\Upsilon} = 0, \quad \psi = 0 \quad \text{at } \Upsilon = 0, \tag{8a}$$

$$\frac{\partial\psi}{\partial\Upsilon} = -h, \quad \psi = q \quad \text{at } \Upsilon = 1. \tag{8b}$$

A. Solution of the fluid problem using a perturbation method

A regular perturbation expansion is used to solve the problem. Solutions for the stream function are assumed in powers of ϵ as

$$\psi(\Sigma,\Upsilon;\epsilon) = \psi^{(0)}(\Sigma,\Upsilon) + \epsilon\psi^{(1)}(\Sigma,\Upsilon) + \epsilon^2\psi^{(2)}(\Sigma,\Upsilon) + \cdots . \tag{9}$$

At this point the small wave number or long-wave approximation, $\epsilon \ll 1$, is introduced. In addition, it is required that $\mathrm{Re} \leq O(1)$, since nonlinear terms are multiplied by Re as well. Substituting the expansion into the governing equations [Eqs. (7) and (8)] and collecting terms of like powers of ϵ, the governing nonlinear equations are reduced to a set of linear equations which can be solved order by order as shown next.

The zeroth-order system $O(\epsilon^0)$ is given by

$$\psi^{(0)}_{\Upsilon\Upsilon\Upsilon\Upsilon} = 0, \tag{10}$$

with the boundary conditions

$$\psi^{(0)}_{\Upsilon\Upsilon} = 0, \quad \psi^{(0)} = 0 \quad \text{at } \Upsilon = 0, \tag{11a}$$

$$\psi^{(0)}_{\Upsilon} = -h, \quad \psi^{(0)} = q \quad \text{at } \Upsilon = 1. \tag{11b}$$

Solving Eq. (10) with boundary conditions (11), the zeroth-order solution is

$$\psi^{(0)} = (h+3q)\frac{\Upsilon}{2} - (h+q)\frac{\Upsilon^3}{2}. \tag{12}$$

The first-order system $O(\epsilon)$ is given by

$$\psi^{(1)}_{\Upsilon\Upsilon\Upsilon\Upsilon} = h\,\mathrm{Re}(\psi^{(0)}_{\Upsilon}\psi^{(0)}_{\Sigma\Upsilon\Upsilon} - \psi^{(0)}_{\Sigma}\psi^{(0)}_{\Upsilon\Upsilon\Upsilon}) - 2h'\mathrm{Re}\psi^{(0)}_{\Upsilon}\psi^{(0)}_{\Upsilon\Upsilon}, \tag{13}$$

with the boundary conditions

$$\psi^{(1)}_{\Upsilon\Upsilon} = 0, \quad \psi^{(1)} = 0 \quad \text{at } \Upsilon = 0, \tag{14a}$$

$$\psi^{(1)}_{\Upsilon} = 0, \quad \psi^{(1)} = 0 \quad \text{at } \Upsilon = 1. \tag{14b}$$

Solving Eq. (13) with boundary conditions (14), the first-order solution is

$$\psi^{(1)} = \frac{\mathrm{Re}\,h'}{280}(3h^2+11hq+15q^2)\Upsilon - \frac{\mathrm{Re}\,h'}{280}(8h^2+27hq + 33q^2)\Upsilon^3 + \frac{\mathrm{Re}\,h'}{40}(h^2+3hq+3q^2)\Upsilon^5 - \frac{\mathrm{Re}\,h'}{560}(4h^2+10hq+6q^2)\Upsilon^7. \tag{15}$$

The second-order system $O(\epsilon^2)$ is given by

$$\psi^{(2)}_{\Upsilon\Upsilon\Upsilon\Upsilon} = h\,\mathrm{Re}(\psi^{(0)}_{\Upsilon}\psi^{(1)}_{\Sigma\Upsilon\Upsilon} - \psi^{(0)}_{\Sigma}\psi^{(1)}_{\Upsilon\Upsilon\Upsilon} + \psi^{(1)}_{\Upsilon}\psi^{(0)}_{\Sigma\Upsilon\Upsilon} - \psi^{(1)}_{\Sigma}\psi^{(0)}_{\Upsilon\Upsilon\Upsilon}) - 2\,\mathrm{Re}h'(\psi^{(0)}_{\Upsilon}\psi^{(1)}_{\Upsilon\Upsilon} + \psi^{(1)}_{\Upsilon}\psi^{(0)}_{\Upsilon\Upsilon}) - 12(h')^2(\psi^{(0)}_{\Upsilon\Upsilon} + \Upsilon\psi^{(0)}_{\Upsilon\Upsilon\Upsilon}) + 2hh''(2\psi^{(0)}_{\Upsilon\Upsilon} + \Upsilon\psi^{(0)}_{\Upsilon\Upsilon\Upsilon}) + 4hh'(2\psi^{(0)}_{\Sigma\Upsilon\Upsilon} + \Upsilon\psi^{(0)}_{\Sigma\Upsilon\Upsilon\Upsilon}) - 2h^2\psi^{(0)}_{\Sigma\Sigma\Upsilon\Upsilon}, \tag{16}$$

with the boundary conditions

$$\psi^{(2)}_{\Upsilon\Upsilon} = 0, \quad \psi^{(2)} = 0 \quad \text{at } \Upsilon = 0, \tag{17a}$$

$$\psi^{(2)}_{\Upsilon} = 0, \quad \psi^{(2)} = 0 \quad \text{at } \Upsilon = 1. \tag{17b}$$

Solving Eq. (16) with boundary conditions (17), the second-order solution is

$$\psi^{(2)} = \left(\frac{a_5}{120} + \mathrm{Re}^2\left[\frac{a_1}{1980} + \frac{a_2}{1008} + \frac{a_3}{420} + \frac{a_4}{120}\right]\right)\Upsilon - \left(\frac{a_5}{60} + \mathrm{Re}^2\left[\frac{a_1}{1584} + \frac{a_2}{756} + \frac{a_3}{280} + \frac{a_4}{60}\right]\right)\Upsilon^3 + \left(\frac{a_5 + \mathrm{Re}^2 a_4}{120}\right)\Upsilon^5 + \frac{\mathrm{Re}^2}{840}a_3\Upsilon^7 + \frac{\mathrm{Re}^2}{3024}a_2\Upsilon^9 + \frac{\mathrm{Re}^2}{7920}a_1\Upsilon^{11}, \tag{18}$$

where $a_1, a_2, \ldots, a_5$ are given in Appendix A.

The perturbation solution up to second order will be employed for the analysis so that

$$\psi(\Sigma,\Upsilon;\epsilon,\phi,\mathrm{Re},q) \equiv \psi^{(0)} + \epsilon\psi^{(1)} + \epsilon^2\psi^{(2)}. \tag{19}$$

Using the zeroth-, first-, and second-order terms, Eqs. (12), (15), and (18), respectively, the assembled solution is

$$\psi = \left\{\frac{h+3q}{2} + \epsilon\frac{\mathrm{Re}\,h'}{280}[3h^2+11hq+15q^2] + \epsilon^2\left[\frac{a_5}{120} + \mathrm{Re}^2\left(\frac{a_1}{1980} + \frac{a_2}{1008} + \frac{a_3}{420} + \frac{a_4}{120}\right)\right]\right\}\Upsilon - \left\{\frac{q+h}{2} - \epsilon\frac{\mathrm{Re}\,h'}{280}[8h^2+27hq+33q^2] + \epsilon^2\left[\frac{a_5}{60} + \mathrm{Re}^2\left(\frac{a_1}{1584} + \frac{a_2}{756} + \frac{a_3}{280} + \frac{a_4}{60}\right)\right]\right\}\Upsilon^3 + \left\{\epsilon\frac{\mathrm{Re}\,h'}{40}[h^2+3hq+3q^2] + \epsilon^2\left[\frac{a_5 + \mathrm{Re}^2 a_4}{120}\right]\right\}\Upsilon^5 - \left\{\epsilon\frac{\mathrm{Re}\,h'}{560}[4h^2+10hq+6q^2] - \epsilon^2\frac{\mathrm{Re}^2}{840}a_3\right\}\Upsilon^7 + \epsilon^2\frac{\mathrm{Re}^2}{3024}a_2\Upsilon^9 + \epsilon^2\frac{\mathrm{Re}^2}{7920}a_1\Upsilon^{11}. \tag{20}$$

The stream function in the physical space is obtained by using $(\Sigma,\Upsilon)\rightarrow(x,y/h)$. The fluid velocities in the moving frame are (u,v), where $u=\partial\psi/\partial y$ and $v=-\partial\psi/\partial x$, these velocity components are related to the fixed frame components by $U=u+1$ and $V=v$, and the coordinate change by $x=X-t$ and $y=Y$.

B. Pressure gradient–flow rate relations

Since the flow is steady in the moving frame, one can characterize the pumping performance by means of the pressure rise per wavelength. The governing equation for the axial pressure gradient is given by

$$p_x = u_{yy} + \epsilon^2 u_{xx} - \epsilon\,\mathrm{Re}[vu_y + uu_x]. \tag{21}$$

We assume a perturbation expansion of the axial pressure gradient as given by

$$p_x = p_x^{(0)} + \epsilon p_x^{(1)} + \epsilon^2 p_x^{(2)} + \cdots . \tag{22}$$

Inserting this expansion into Eq. (21), the following set of equations is obtained:

(i) for $O(\epsilon^0)$

$$p_x^{(0)} = u_{0yy}, \tag{23}$$

(ii) for $O(\epsilon^1)$

$$p_x^{(1)} = u_{1yy} - \mathrm{Re}[v_0 u_{0y} + u_0 u_{0x}], \tag{24}$$

(iii) for $O(\epsilon^2)$

$$p_x^{(2)} = u_{0xx} + u_{2yy} - \mathrm{Re}[v_0 u_{1y} + v_1 u_{0y} + u_0 u_{1x} + u_1 u_{0x}]. \tag{25}$$

The zeroth-, first-, and second-order velocities are introduced in terms of the stream function obtained in Sec. II A for the axial velocities $u_j = \partial\psi^{(j)}/\partial y$ and for the transverse velocities $v_j = -\partial\psi^{(j)}/\partial x$, with $j=0,1,2$. The pressure gradient is known at each order by substituting each velocity in Eqs. (23)–(25). Now, a nondimensional pressure gradient per wavelength is defined so that

$$\Delta P_\lambda \equiv \int_0^{h(x=0)} \left(\int_0^\lambda \frac{\partial p}{\partial x} dx \right) dy. \tag{26}$$

Using the pressure gradient at each order, a pressure change per wavelength is calculated as

$$\Delta P_\lambda \equiv \Delta P_0 + \epsilon \Delta P_1 + \epsilon^2 \Delta P_2, \tag{27}$$

where $\Delta P_j = \int_0^{h(x=0)} (\int_0^\lambda p_x^{(j)} dx) dy$, with $j=0,1,2$. By introducing terms at each order, a pressure change per wavelength up to second order is obtained, and integrating from 0 to π gives

$$\begin{aligned}
\Delta P_\lambda = & -3I_2 - 3I_3 q + \frac{\epsilon \mathrm{Re}}{35}\{54 I_{p3} q^2 + 6 I_{p2} q - 6 I_{p1}\} \\
& + \epsilon^2 \left\{ \frac{\mathrm{Re}^2}{13475}(624 I_{2p3} - 468 I_{pp2}) q^3 + \frac{\mathrm{Re}^2}{13475}(52 I_{2p2} \right. \\
& \left. - 632 I_{pp1}) q^2 - \frac{\mathrm{Re}^2}{5775}(132 I_{2p1} + 127 I_{pp0}) q \right\} \\
& + \epsilon^2 \left\{ (60 I_{2p5} - 15 I_{pp4} + 3 I_{pp2} - 42 I_{2p3}) \frac{q}{10} \right. \\
& \left. - \frac{\mathrm{Re}^2}{40425}(166 I_{pp(-1)} + 363 I_{2p0}) - \frac{18}{5} I_{2p2} \right\} \\
& + \epsilon^2 \left\{ 3 I_{2p4} + \frac{6}{5} I_{pp1} - I_{pp3} \right\},
\end{aligned} \tag{28}$$

where the I's are given in Appendix B. The pumping performance ΔP_λ vs Q can be inspected by substituting $q = Q + \phi/2 - 1$. In the analysis, integrations were performed numerically because of the nature of the wave form h.

III. PARTICLE EQUATION OF MOTION IN A NONUNIFORM FLOW

The BBO equation for motion of a small rigid sphere in a nonuniform flow at low Reynolds numbers [25,30] in dimensional form is given by

$$\begin{aligned}
m_p \frac{d\bar{U}_p^*}{dt^*} = & (m_p - m_f)\bar{g}^* + m_f \frac{D\bar{U}_f^*}{Dt^*} - \frac{1}{2} m_f \frac{d}{dt} \left\{ \bar{U}_p^* - \bar{U}_f^* \right. \\
& \left. - \frac{a^2}{10} \breve{\nabla}^{*2} \bar{U}_f^* \right\} - 6\pi a \mu \left\{ \bar{U}_p^* - \bar{U}_f^* - \frac{a^2}{6} \breve{\nabla}^{*2} \bar{U}_f^* \right\} \\
& - 6\pi a^2 \mu \left[\int_0^{t^*} \frac{\frac{d}{dt^*}(\bar{U}_p^* - \bar{U}_f^*) dt'}{\sqrt{\pi \nu (t^* - t')}} \right],
\end{aligned} \tag{29}$$

where $\bar{U}_f^* = \{U, V\}$ is the fluid velocity vector, $\bar{U}_p^* = \{U_p, V_p\}$ is the particle velocity vector, $\bar{g}$ is the gravity vector, m_f is the mass of the fluid with the same volume as the sphere, m_p is the particle mass, $a = d_p/2$ is the particle radius, μ is the fluid dynamic viscosity, ν is the fluid kinematic viscosity, and t^* is the time. The BBO equation represents the sum of steady-state drag force, the pressure or buoyancy force, the virtual mass force, the Basset force, and the body force equated to the mass times the acceleration of an isolated particle.

Dimensionless quantities are defined as $X \equiv \pi X^*/\lambda$ and $Y \equiv Y^*/R_w$ for the spatial coordinates. For the velocities $U \equiv U^*/c$ and $V \equiv V^*/c$, $U_p \equiv \bar{U}_p^*/c$ and $V_p \equiv V_p^*/c$, for the time $t \equiv t^*/\tau_c$, and for the gravity $\bar{g} \equiv \bar{g}^*/g_0$. The fluid characteristic time is defined as $\tau_c \equiv \lambda/(\pi c)$ and the particle relaxation time as $\tau_p = \rho_p d_p^2/(18\mu)$. The nondimensional BBO equation with its force terms per particle mass is given by

$$\begin{aligned}
\underbrace{\frac{d\bar{U}_p}{dt}}_{\text{acceleration}} = & \underbrace{\frac{1}{\mathrm{St}}\left(\frac{2S}{2S+1}\right)(\bar{U}_f - \bar{U}_p)}_{\text{Stokes drag}} + \underbrace{\frac{3}{2S+1}\frac{d\bar{U}_f}{dt}}_{\text{virtual mass}_1} + \underbrace{\frac{\alpha^2}{40(2S+1)}\frac{d}{dt}\breve{\nabla}^2 \bar{U}_f}_{\text{virtual mass}_2} + \underbrace{\frac{\alpha^2}{24\mathrm{St}}\left(\frac{2S}{2S+1}\right)\breve{\nabla}^2 \bar{U}_f}_{\text{Faxén}} \\
& + \underbrace{\sqrt{\frac{9}{2\pi S \mathrm{St}}\left(\frac{2S}{2S+1}\right)} \left[\int_0^t \frac{\frac{d}{dt}(\bar{U}_f - \bar{U}_p) dt'}{\sqrt{t-t'}} + \frac{\bar{U}_{f0} - \bar{U}_{p0}}{\sqrt{t}} \right]}_{\text{Basset}} + \underbrace{\left(\frac{2(S-1)}{2S+1}\right)\frac{g_0 \tau_c}{c}\bar{g}}_{\text{gravity}},
\end{aligned} \tag{30}$$

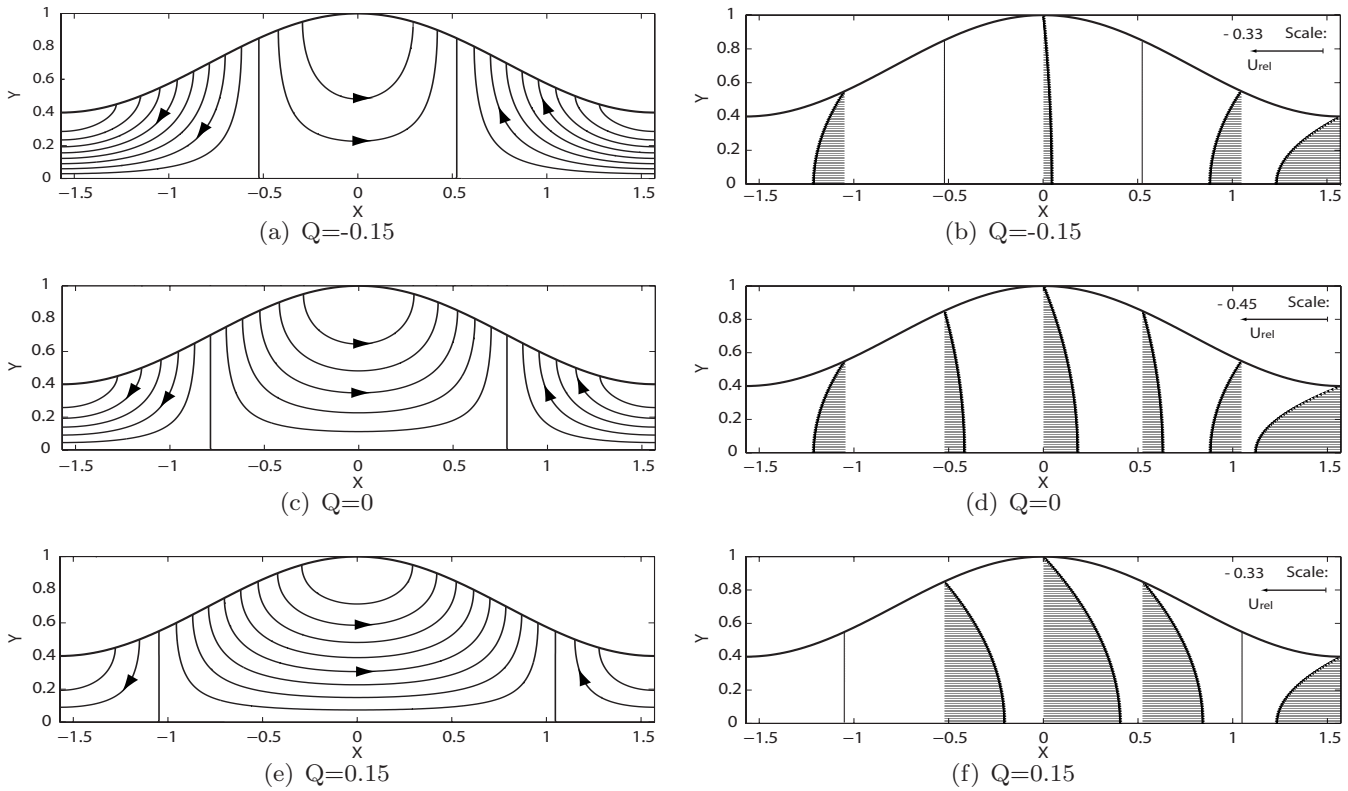

FIG. 2. [(a), (c), and (e)] fluid instantaneous streamlines and [(b), (d), and (f)] axial velocity profiles in a fixed frame at $t=0$ for different values of Q with parameters $\{\mathrm{Re}=0(\mathrm{Re}_m=0);\phi=0.6;\epsilon=0.1\}$. The scaling $U_{\mathrm{rel}}=U/[0.75\langle U(X=0)\rangle_{\mathrm{mean}}]$.

where $S\equiv\rho_p/\rho_f$ is the density ratio, $\mathrm{St}\equiv\tau_p/\tau_c$ is the Stokes number, $\alpha\equiv d_p/R_w$ is the size ratio, and the nondimensional Laplacian $\breve{\nabla}^2\equiv\epsilon^2\partial^2/\partial X^2+\partial^2/\partial Y^2$. The six terms on the right-hand side of the nondimensional BBO equation are (from left to right) the forces due to Stokes drag (first term), virtual mass (second and third terms), Faxén (fourth term), Basset (fifth term), and gravity (sixth term). This equation will be used to study the particle motion in a peristaltic fluid flow.

When particles are nonspherical, their drag differs from the Stokes drag. This can be accounted for by the dynamic shape correction factor ξ in

$$F_{\mathrm{drag}}=3\pi d_p\mu\xi(\bar{U}_f^*-\bar{U}_p^*), \tag{31}$$

where d_p now represents the diameter of a sphere with the same volume and velocity as the nonspherical particle; ξ is typically between 1 and 2. Experimental estimates of dynamic shape correction factors for diverse geometric shapes are [31] as follows: for a sphere $\xi=1$, for a cube $\xi=1.08$, and for a cluster of spheres $\xi=1.12$ (two chained), $\xi=1.27$ (three chained), and $\xi=1.15$ (three compact). Thus, the force due to Stokes drag is modified as $\frac{\xi}{\mathrm{St}}(\frac{2S}{2S+1})(\bar{U}_f-\bar{U}_p)$.

In Sec. IV, spherical and nonspherical particles will be analyzed using the BBO equation and the influence of the parameters $\{\epsilon;\phi;\mathrm{Re};Q;\alpha;S;\mathrm{St}\}$ for the particle-laden fluid-peristalsis problem.

IV. RESULTS AND DISCUSSION

A. Fluid mechanics: Streamlines, velocity profiles, and pumping characteristics

The results of the analysis are presented as follows: (a) streamlines and velocity profiles for the parameters $\{\epsilon;\phi;\mathrm{Re};Q\}$; (b) the pressure gradient–flow rate relationship for the parameters $\{\epsilon;\phi;\mathrm{Re}\}$; and (c) comparison of the analytical solution up to second order in ϵ^2 with experimental data. A modified Reynolds number, $\mathrm{Re}_m\equiv\epsilon\mathrm{Re}$, is used since it characterizes the peristaltic fluid flow problem well.

Streamlines and the corresponding axial velocity profiles in the fixed frame at $t=0$ are shown in Figs. 2 and 3. Figures 2(a)–2(f) are plotted for the parameter values $\{\epsilon=0.1;\phi=0.6;\mathrm{Re}=0\}$. As the flow rate becomes positive, the region of downward-upward streamlines below the wave crest increases as well. In maintaining the flow rate fixed with $\{\epsilon=0.1;\phi=0.6;Q=0\}$ [Figs. 3(a)–3(f)], the influence of the Reynolds number on the flow structure can be noted. As seen in the velocity profiles, the nonuniformity of the flow is evident near the wave trough in which flow enters.

Figures 4(a) and 4(b) present the nondimensional pressure gradient per wavelength (ΔP_λ) vs the dimensionless flow rate (Q). The graphs are sectored: quadrant I denotes the region of peristaltic pumping where $Q>0$ (positive pumping) and $\Delta P_\lambda>0$ (adverse pressure gradient); quadrant II is where $\Delta P_\lambda<0$ (favorable pressure gradient) and $Q>0$ (positive pumping) is augmented flow; and in quadrant IV, $\Delta P_\lambda>0$ (adverse pressure gradient) and $Q<0$ is backward

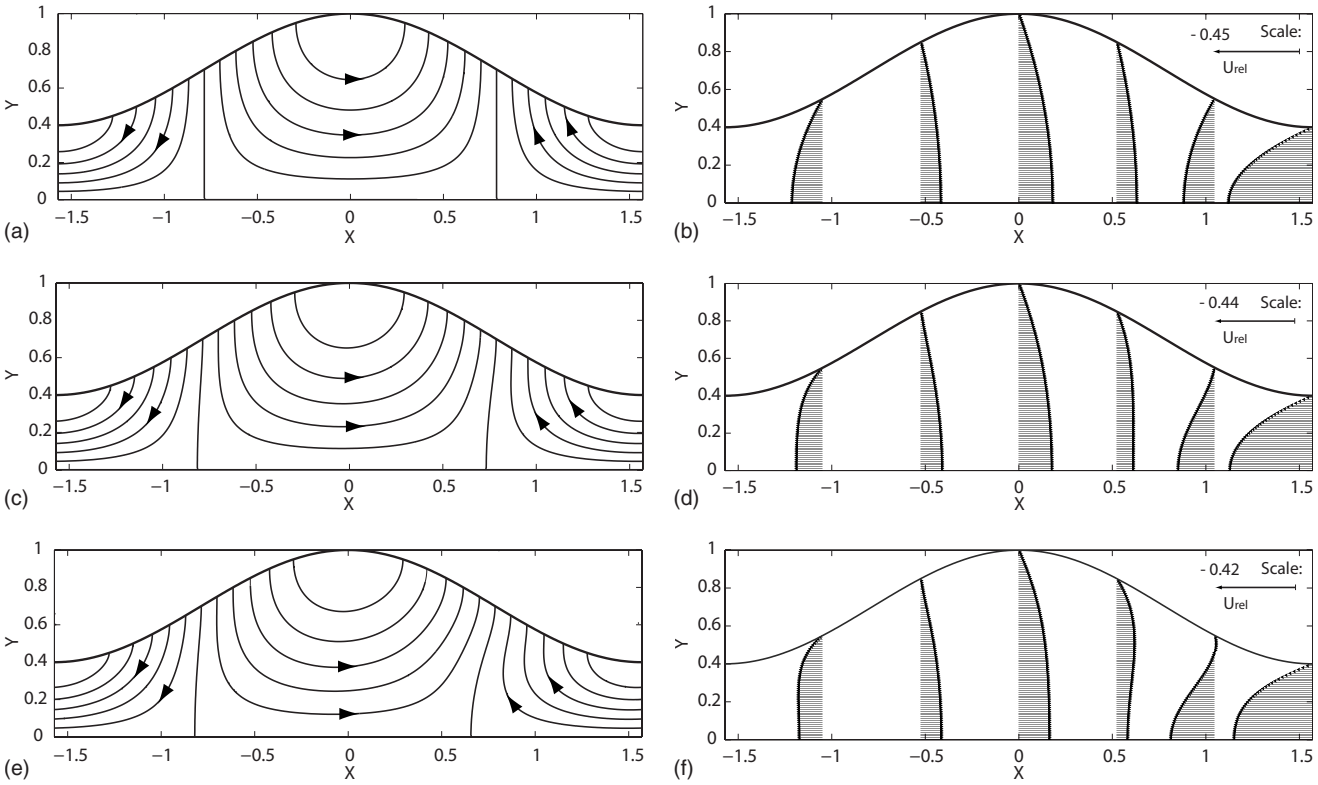

FIG. 3. (a) Re=0(Re$_m$=0), (b) Re=0(Re$_m$=0), (c) Re=50(Re$_m$=5), (d) Re=50(Re$_m$=5), (e) Re=100(Re$_m$=10), and (f) Re=100(Re$_m$=10) Fluid instantaneous streamlines and [(b), (d), and (f)] axial velocity profiles for a fixed frame at $t=0$ for different values of Re with parameters $\{\phi=0.6;\epsilon=0.1;Q=0\}$. The scaling $U_{\mathrm{rel}}=U/[0.75\langle U(X=0)\rangle_{\mathrm{mean}}]$.

pumping [29]. For the upper half plane, there is an adverse pressure gradient acting against the peristaltic action. In contrast, in the lower half plane, the pressure gradient is favorable and acts in the same direction as peristalsis. Figures 4(a) and 4(b) are traced for $\{\epsilon=0.1;\phi=0.6,0.9;\mathrm{Re}=0,100\}$. As required by the linear nature of the problem for zero Reynolds number, the curve of ΔP_λ vs Q is a straight line with negative slope, as shown in Fig. 4(a). In Fig. 4(a) the effect of the Reynolds number is to increase the slope of the pumping curve; note that the value of $(Q)_{\Delta P_\lambda=0}$ also decreases. For an almost occluded wave with $\phi=0.9$ [Fig. 4(b)], the nonlinear effect of the Reynolds number in the pumping curve is evident.

Weinberg *et al.* [13,32] carried out experimental investigations of a two-dimensional peristaltic flow induced by sinusoidal waves. Measurements of mean flow, mean pressure rise, and pressure pulses were made. Their work was concerned with low Reynolds numbers ranging from the inertia-free limit to values in which inertial effects are significant. The experimental apparatus was a pumping duct with rectangular cross section and bounded by a rigid semicircular back wall. A flexible moving wall was driven by roller cams, producing longitudinal waves of transverse displacement. Peristaltic action of the moving wall was created by using a cam assembly to generate a traveling sinusoidal wave. In Figs. 5 and 6, the perturbation solution up to order ϵ^2 is compared with the experimental data of Weinberg *et al.* [13]. The dashed line in each graph is the expansion solution of [13] up to terms of order Re_m^2, which was based on an asymptotic approach using the modified Reynolds number as the perturbation parameter. In the experiments, the Reynolds number was varied using fluids of different viscosity and different wave speeds. It is important to mention that the calculations of Weinberg *et al.* [13] were performed with a wave form given by $H_{\mathrm{expt}}=1+\phi\sin 2\pi(X-t)$ and, consequently, their time–mean flow rate was $Q_{\mathrm{expt}}=q+1$. The terms of the pressure gradient were integrated from 0 to 1, and the modified Reynolds number was used.

Figure 5 shows the relation between the maximum pressure change per wavelength, $(\Delta P_{\mathrm{max}})_{\mathrm{expt}}\equiv(\Delta P_\lambda)_{Q_{\mathrm{expt}}=0}$ and $(\mathrm{Re}_m)_{\mathrm{expt}}$. Figure 6 shows the time–mean flow rate for zero pressure change $(Q_0)_{\mathrm{expt}}\equiv(Q_{\mathrm{expt}})_{\Delta P_\lambda=0}$ vs $(\mathrm{Re}_m)_{\mathrm{expt}}$; the points are experimental data of Weinberg *et al.* [13] and the dashed line is his analytical approximation. An important indication from Fig. 5 is that the present second-order expansion agrees with the conclusions of Weinberg *et al.* [13] for $\mathrm{Re}_m\cong 10$. Figure 6 shows certain deviations from the data. Weinberg *et al.* [13] argued that these deviations were due to problems with the measurements since the pressure rise within the apparatus was relatively small for high $(\mathrm{Re}_m)_{\mathrm{expt}}$, and fluctuations in the reservoir introduced relative errors when operating with nominally equal reservoir levels for zero pressure change. The experimental observation of $(Q_0)_{\mathrm{expt}}$ at high $(\mathrm{Re}_m)_{\mathrm{expt}}$ involved errors, which were estimated as being at most $\pm 5\%$ for the data shown in Fig. 6.

Based on agreement with experiments, one can say that the analysis is valid for $\mathrm{Re}_m\leq 10$ so that it appears that the range of validity of the $O(\epsilon^2)$ solution is larger than what can

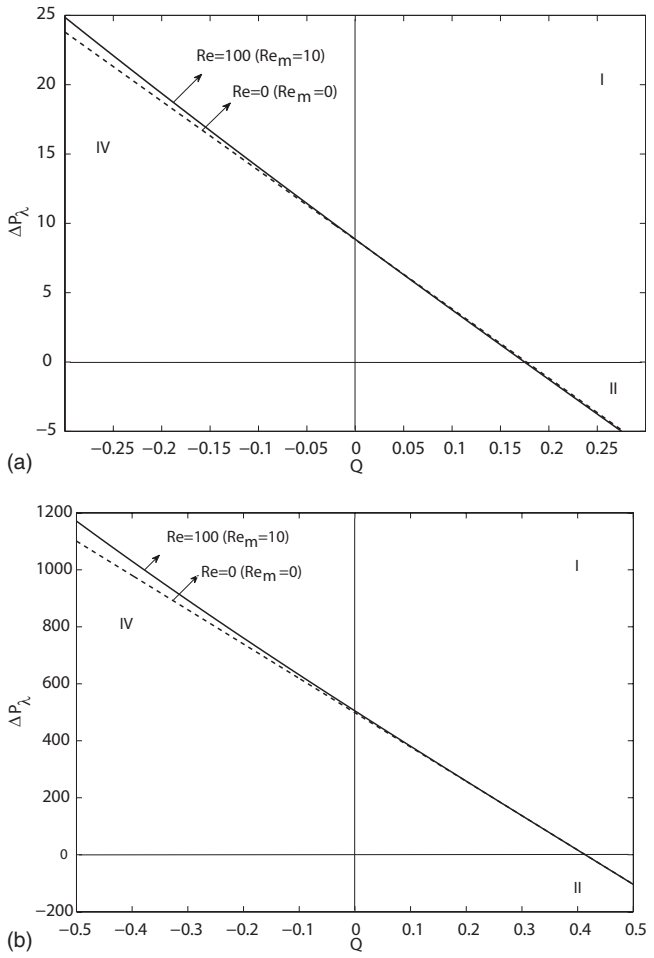

FIG. 4. (a) $\phi=0.6$ and (b) $\phi=0.9$ Pumping curves for different Reynolds numbers with geometrical parameters $\epsilon=0.1$ and ϕ.

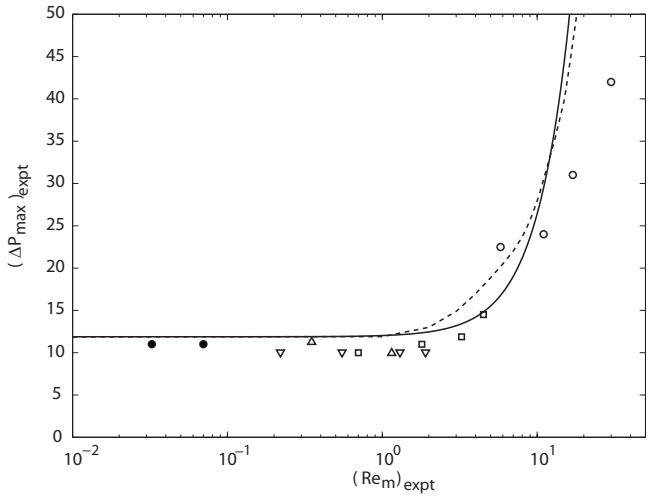

FIG. 5. Effect of the Reynolds number on the maximum pressure rise with $\epsilon=0.014$ and $\phi=0.7$. Data points are from the experiments of Weinberg *et al.* [13]. Dashed curve is theory based on second-order expansion in Re_m of Weinberg *et al.* [13]. Solid line is present solution up to a second-order expansion in ϵ. Viscosities in centipoise: ○, 1; □, 6; ▽, 12; △, 14; and ●, 150.

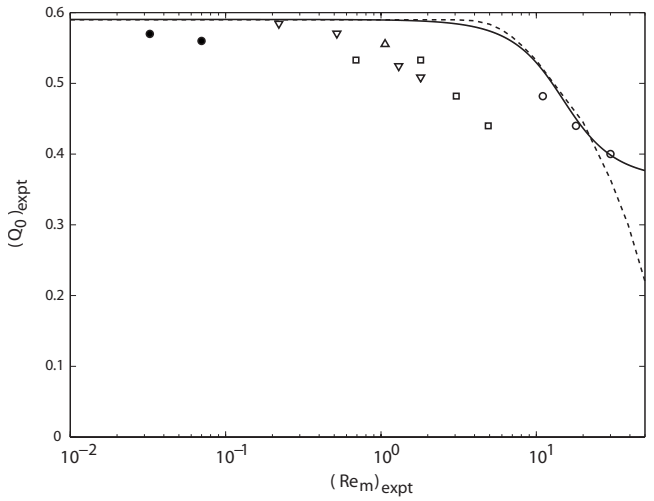

FIG. 6. Effect of the Reynolds number on the time–mean flow rate for zero pressure change. Dashed curve is theory based on second-order expansion in Re_m of Weinberg *et al.* [13]. Solid line is present solution up to a second-order expansion in ϵ. Viscosities in centipoise: ○, 1; □, 6; ▽, 12; △, 14; and ●, 150.

be expected *a priori*. This is due to the fact that the higher-order terms decrease rapidly in magnitude, and the convergence of the series is quite good even when $\mathrm{Re}_m > O(1)$. Looking at it further, it is found that $\mathrm{Re}_m = \epsilon \mathrm{Re} = (\pi R_w/\lambda) c R_w/\nu = \omega R_w^2/\nu$, where $\omega = \pi c/\lambda$. Following Jaffrin and Shapiro [2], if a frequency parameter $\beta = R_w\sqrt{\omega/\nu}$ is defined, where ω is the wave angular frequency, then it turns out that $\mathrm{Re}_m = \beta^2$. Therefore the value of Re_m characterizes also the ratio of vorticity diffusion time over length R_w to the period of the wave. In the limit of $\mathrm{Re}_m \to 0$, the flow is inertia free and thus has Poiseuille-type instantaneous velocity profiles. At the other limit, when $\mathrm{Re}_m \to \infty$, oscillating Rayleigh boundary layers develop, with instantaneous velocity profiles that are nearly uniform over most of the cross section. This means that $\mathrm{Re}_m \leq 10$, is valid for long-wavelength and low-frequency problems.

B. Application to biomechanics: Particle motion in ureteral peristaltic flow

The urinary system shown in Fig. 7 consists of the kidneys, ureters, bladder, and urethra. It can be divided into two sections, an upper (kidneys to ureters) and a lower (bladder to urethra) section. As mentioned in Sec. I, under normal conditions, urine flows from the kidneys to the bladder by peristaltic action of the ureteral wall. In an adult human, typical ureteral dimensions and bolus velocity, as suggested for biomechanical modeling by Boyarski *et al.* [33], are $R_w = 2.5$ mm, $\lambda = 120$ mm, and $c = 30$ mm/s. Urine characteristics are similar to that of water so that the density is $\rho \cong 1000$ kg/m^3 and viscosity $\mu \cong 0.000\,89$ N s/m^2 at ambient conditions. The major assumption in the present analysis is a two-dimensional geometry with the wall being represented as an infinite train of sinusoidal waves. Complete occlusion does not occur in the cases analyzed here. The fluid being transported is incompressible and Newtonian, and the

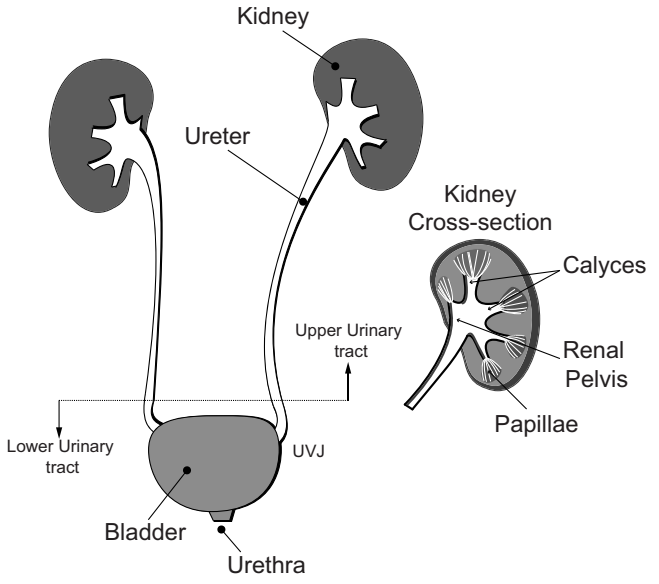

FIG. 7. Schematic of the urinary system and cross section of the kidney.

process occurs at isothermal conditions. Parameter values used are $\epsilon=0.0654$ and $\mathrm{Re}=84.27$, which gives $\mathrm{Re}_m \approx 5.5$.

The value of $Q_0 \equiv (Q)_{\Delta P_\lambda=0}$ (free pumping) is of particular physiological relevance since it represents peristalsis without a prescribed pressure gradient. In abnormal situations, lower or higher fractions of this pressure gradient may occur. In Fig. 8, Q vs ϕ is presented for the parameters of ureteral peristalsis. Three regions divide the graph: retrograde ($Q<0$), trapping ($0<Q<Q_0$), and augmented flow ($Q>Q_0$). The lines correspond to zero ($Q=0$) and free pumpings (Q_0). For $\phi=0$ (no peristalsis), there is no time–mean flow; for $\phi=1$ (complete occlusion) $Q=1/2$. Moreover, the dimensional time–mean flow rate for $\phi=1$ is $\hat{Q}=R_w c$. This is the volume flow that would be pumped if all the liquid inside the bolus was transported as a rigid body rightward at speed c.

There exist situations in which peristalsis occurs with solid particles in the fluid. One is when minerals precipitate

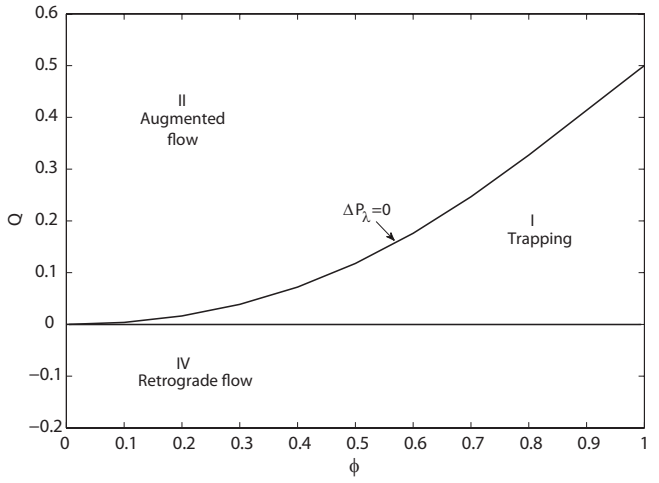

FIG. 8. Regions of trapping or separated flows with parameters $\epsilon=0.0654$ and $\mathrm{Re}=84.27$.

in the kidneys to form small crystals, commonly called ureteral calculi or stones. A mixture of the fluid and particles, the most common being calcium oxalates (CaOx) [34,35], is then transported along the ureter. Urine dilution has been considered as a tool in the prevention of calcium renal stones. Moreover, if stones grow to sufficient size before passage, on the order of at least 2–3 mm, they obstruct the ureter. Under this pathology, the use of extracorporeal shock wave lithotripsy (ESWL) has become a standard treatment of calculosis. ESWL refers to the use of an extracorporeal acoustic generator to break up the stones into smaller pieces that are easier to transport along the ureter. After treatment with ESWL, a fluid particle mixture has to be transported along the ureter. It has been reported that residuals from the upper urinary tract calculi have sometimes failed to clear after successful ESWL, thereby causing regrowth [36,37]. In a diluted urine mixture, the particle diameter of CaOx is approximately 10.2 μm, as reported in [38], and the average density of these crystals is approximately 1960 $\mathrm{kg/m^3}$ [39]. This section investigates the fate and influence of a particle-fluid mixture on ureteral peristalsis.

Another important example of immersed bodies is bacteriuria, which is the presence of bacteria in urine. Urinary tract infections can occur as a consequence of this condition. In the upper urinary tract, it has been hypothesized that bacteria are sometimes transported in a direction opposite to the peristaltic action, and authors have concluded [40,41] that reflux can possibly be responsible for some infections in the kidney. It is common that reflux appears in ureterovesical junction (UVJ), which allows passage of urine from the ureter into the bladder and prevents flow in the reverse direction. If the valvular mechanism is defective, the urine flows back into the ureter and kidney, creating a condition known as vesicoureteral reflux (VUR) [42,43]. These conditions motivate the study of bacterial peristaltic transport. A common bacterium found in urine is *Escherichia coli* (*E. coli*), with the approximate dimensions 1×2 $\mu\mathrm{m}^2$ [44] and a density of $\rho_p=1160$ $\mathrm{kg/m^3}$ [45]. In the present paper, $d_p=1$ μm and a two-chain correction factor $\xi=1.12$ are used for bacteria.

In Sec. IV B 1 two situations are analyzed: peristaltic transports of a fluid with CaOx particles and with bacteria. In Table I the values of the particle parameters $\{S;\alpha;\mathrm{St}\}$ are presented, and an estimate of the order of each term in the BBO equation is included.

1. Particle motion of spherical and nonspherical particles in low-Reynolds-number peristaltic flow

The system of equations that governs the motion of a nonspherical particle in a nonuniform flow with a low Reynolds number, subjected to gravity in the negative Y direction in a Cartesian coordinate system is

$$\frac{dU_p}{dt} = c_1(U-U_p) + c_2\frac{dU}{dt} + c_3\frac{d}{dt}\breve{\nabla}^2 U + c_4\left[\int_0^t \frac{\frac{d}{dt}(U-U_p)dt'}{\sqrt{t-t'}} + \frac{U_0-U_{p0}}{\sqrt{t}}\right] + c_5\breve{\nabla}^2 U, \tag{32a}$$

TABLE I. Particle parameter values and order of the force terms of the BBO equation.

	CaOx	Bacteria
S	1.96	1.16
α	4.1×10^{-3}	4×10^{-4}
St	9.997×10^{-6}	5.687×10^{-8}
Stokes drag	7.969×10^{4}	1.376×10^{7}
Virtual mass$_1$	0.6098	0.936
Virtual mass$_2$	8.458×10^{-8}	1.204×10^{-9}
Basset	215.42	3.256×10^{3}
Faxén	0.055	0.0819
Gravity	162.48	40.116

$$\frac{dV_p}{dt} = c_1(V - V_p) + c_2\frac{dV}{dt} + c_3\frac{d}{dt}\breve{\nabla}^2 V + c_4\left[\int_0^t \frac{\frac{d}{dt}(V - V_p)dt'}{\sqrt{t - t'}} + \frac{V_0 - V_{p0}}{\sqrt{t}}\right] + c_5\breve{\nabla}^2 V - c_6, \tag{32b}$$

$$\frac{dX_p}{dt} = U_p, \tag{32c}$$

$$\frac{dY_p}{dt} = V_p, \tag{32d}$$

where $c_1=\frac{\xi}{\mathrm{St}}(\frac{2S}{2S+1})$, $c_2=\frac{3}{2S+1}$, $c_3=\frac{\alpha^2}{40(2S+1)}$, $c_5=\frac{\alpha^2}{24\mathrm{St}}(\frac{2S}{2S+1})$, $c_4=\sqrt{\frac{9}{2\pi S\mathrm{St}}}(\frac{2S}{2S+1})$, and $c_6=(\frac{2(S-1)}{2S+1})\frac{g_0\tau_c}{c}$. Suitable alterations can be made for gravity in other directions. For $\xi=1$, the spherical geometry is recovered.

The system of differential equations [Eqs. (32)] was integrated numerically to obtain the particle position in time, given initial conditions for different values of the parameters. This particle tracking is done in the Lagrangian point of view. The numerical integration of the Basset force term was performed using an approximation for the Basset integral [46], in which $\int_0^t (dv/dt)d\tau/(\sqrt{t-\tau}) \approx (v-v_0)/\sqrt{0.5t}$. This formula represents the mean value theorem for a definite integral with $\tau=0.5t$ as an average value.

Comparisons between the trajectories of a CaOx particle and the bacteria type are shown in Figs. 9(a) and 9(b). Four situations are investigated for the particle motion subjected to peristaltic flow: retrograde flow ($Q<0$), zero pumping ($Q=0$), free pumping [$Q_0\equiv(Q)_{\Delta P_\lambda=0}$], and augmented flow ($Q>Q_0$). The calculations were performed by specifying an initial position and a zero initial velocity. The time is measured in units of π, so that $T\equiv t/\pi$.

Figure 9(a) shows the particle trajectories for CaOx and bacteria for retrograde motion: all particles go in the direction opposite to peristaltic action. CaOx particles near the longitudinal axis follow similar trajectories as the bacteria. However, particles near the wall tend to approach it. Figure 9(b) shows zero pumping: particles near the longitudinal axis have a net positive displacement. In contrast, particles near the wall have a net negative displacement. This corresponds to the reflux situation reported in the classical literature on peristaltic pumping. CaOx and bacteria have similar trajectories near the wall. Near the axis, the similarity is broken, but positive displacement is maintained. Figure 9(c) shows pure peristalsis: particles near the center have a total positive displacement with no oscillations. Particles near the wall oscillate, but with net positive displacement. CaOx particles that travel along the longitudinal axis tend to fall down to the lower wall because of gravity. Figure 9(d) shows the particle trajectories for augmented pumping: particles near the axis tend to acquire a linear translation, and particles near the walls oscillate. The effect of gravity in CaOx particles is more evident when compared to Q_0.

The effect of gravity on the particles, as shown in Figs. 10 and 11, is examined further. Figure 10 shows bacteria for free pumping, Q_0. Whether or not gravity is significant can be seen by comparing its effect when acting in the positive X or negative Y direction. For bacteria, the effect of gravity is insignificant due to its small particle size and low density. Figure 10 corresponds to CaOx, for which there are considerable differences in the particle paths if gravity acts in the negative Y direction rather than in the positive X direction. Particles with gravity in the X direction move symmetrically. In contrast, particle paths with gravity in the negative Y direction are not symmetric. In addition, particles near the upper wall start to fall down, thereby producing a nonzero increment in the net X displacement. Particles near the lower wall move upward. This causes a reduction in the particles' net X displacement.

The retrograde motion or reflux described above for zero pumping, when present, can readily explain the transport of bacteria to the upper urinary tract since the outer liquid layer is displaced in the upstream direction. It is important to mention that, for simplification, bacteria have been considered as passive solid bodies in motion. However, bacteria are known to be organisms with their own motile behavior. For example, *E. coli* has a flagellum that is driven in its base by a reversible rotary motor. The cell's ability to migrate in a particular direction results from change in direction of rotation of this flagellum [47]. However, as mentioned by Shapiro *et al.* [1] and Shapiro [41], the motion of the particles happens much too rapidly to be explained by molecular diffusion alone, even when it is enhanced by bacterial self-propulsion. Shapiro and Jaffrin [48] showed that Lagrangian trajectory calculations should be used to study material reflux. Reflux can occur in the presence of high backpressure, such as in VUR. A computation of a particle in reflux is shown in Fig. 12 for $Q=0$ with the parameters for ureteral peristalsis and $\phi=0.8$ and $\phi=0.99$. Negative net longitudinal displacement is shown in Fig. 13 for both. For $\phi=0.8$, a particle near the wall ($x_0=0$, $y_0=0.9$) moves in the negative direction. If the same parameters are used but with $\phi=0.99$, the particles eventually reach the wall.

Now consider a slight opening in which reflux is possible as, for example, when $\phi=0.8$. An approximation of the particle average axial velocity is $\langle u_p\rangle \equiv \Delta X_p/\Delta t=3.6$ mm/s. Thus, the particle is transported in the negative direction by approximately 12% of the wave velocity ($c=3$ cm/s). Mea-

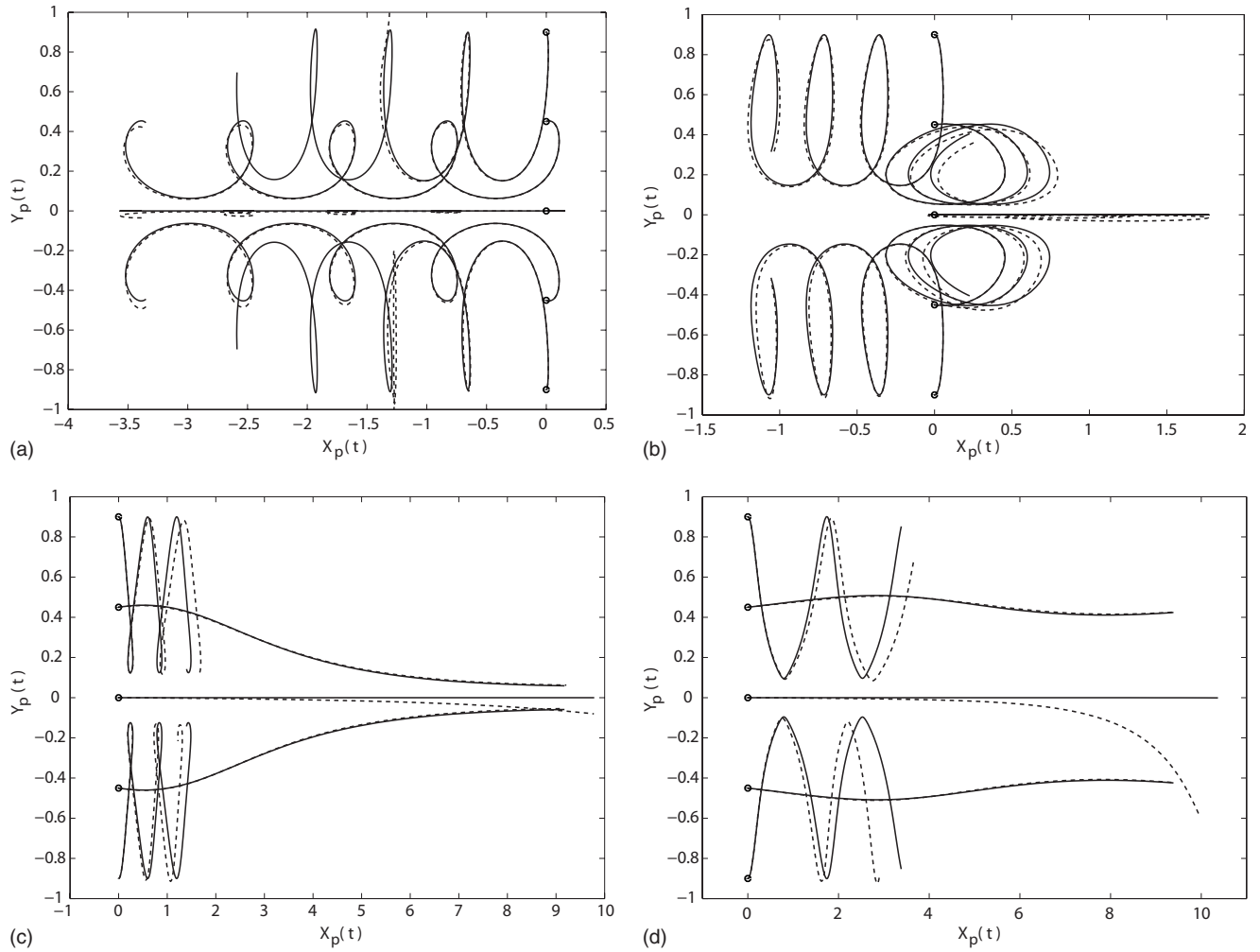

FIG. 9. (a) $Q=-0.2$, retrograde flow; (b) $Q=0$, zero-pumping; (c) $Q_0=0.327$, free pumping; (d) $Q=0.45$, augmented flow. Particle trajectories with the fluid parameters $\{\epsilon=0.0654; \phi=0.8; \mathrm{Re}=84.27\}$ for different values of the time–mean flow rate. Particle parameters: for bacteria, $\{\alpha=0.0004; S=1.16; \mathrm{St}=5.687\times10^{-8}\}$; for CaOx, $\{\alpha=0.0041; S=1.96; \mathrm{St}=9.997\times10^{-6}\}$. Particle initial positions are at $x=0$ on $y=\{0, \pm0.45, \pm0.9\}$, with zero initial velocities, integration carried up to $T=3$. Peristalsis acts in the positive X direction and gravity in the negative Y direction. Particle trajectory: solid line, bacteria; dashed line, CaOx.

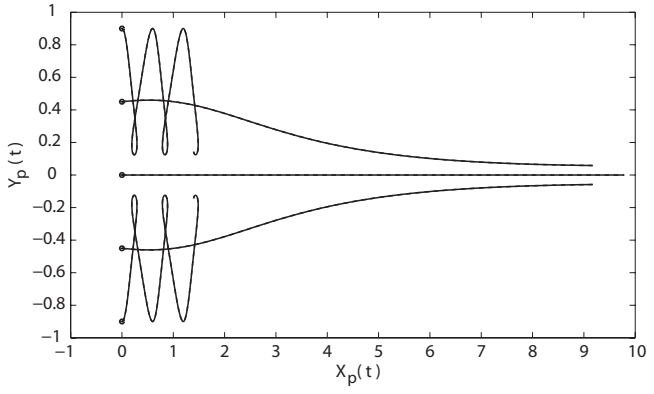

FIG. 10. Effect of gravity on particle motion for bacteria with flow rate $Q_0=0.327$. Fluid and particle parameters $\{\epsilon=0.0654; \phi=0.8; \mathrm{Re}=84.27; \alpha=0.0004; S=1.16; \mathrm{St}=5.687\times10^{-8}\}$. Particle initial positions are $x=0$, $y=\{0, \pm0.45, \pm0.9\}$ with zero initial velocities; integration carried to $T=3$. Solid line is gravity in positive X direction; dashed line is gravity in negative Y direction.

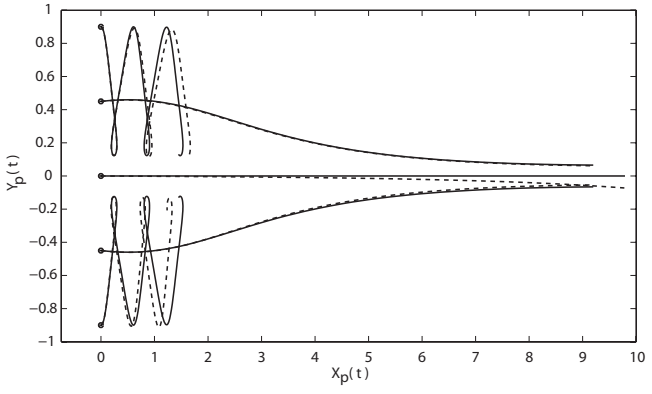

FIG. 11. Effect of gravity on particle motion for CaOx with flow rate $Q_0=0.327$. Fluid and particle parameters $\{\epsilon=0.0654; \phi=0.8; \mathrm{Re}=84.27; \alpha=0.0041; S=1.96; \mathrm{St}=9.997\times10^{-6}\}$. Particle initial positions are $x=0$, $y=\{0, \pm0.45, \pm0.9\}$ with zero initial velocities; integration carried to $T=3$. Solid line is gravity in positive X direction; dashed line is gravity in negative Y direction.

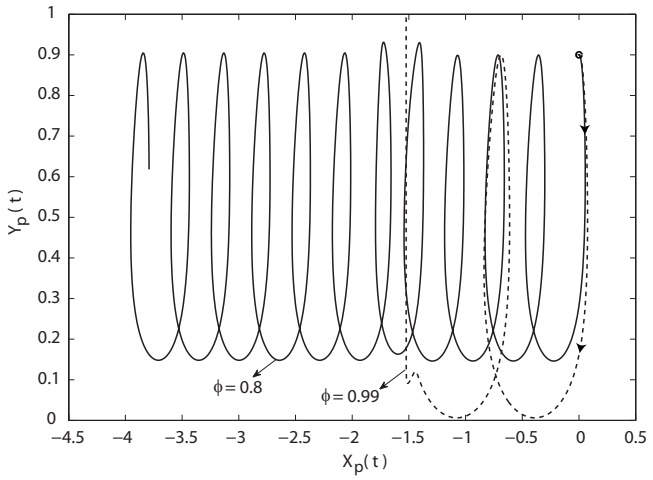

FIG. 12. Particle trajectory for bacteria with $Q=0$ and gravity in positive X direction. Fluid and particle parameters $\{\epsilon=0.0654; \mathrm{Re}=84.27; \alpha=0.0004; S=1.16; \mathrm{St}=5.687\times10^{-8}\}$. Initial position (0,0.9) and zero initial velocity, integration to $T=10$. Solid line is $\phi=0.8$; dashed line is $\phi=0.99$.

surements were made of the single-cell motility for *E. coli* in restricted geometries and bulk flow [49], where the cell speed was found to be approximately 26.2 μm/s. This implies that reflux of bacteria by fluid transport is approximately 137 times faster than self-propulsion, when considering $\langle u_p \rangle$.

All previous calculations were performed considering all terms of the BBO equation. For computational efficiency, some forces may not need to be included. In Figs. 14 and 15, three cases are compared: (a) all forces; (b) Stokes drag, Basset, and gravity; and (c) Stokes drag and gravity. Estimates of the orders of all the forces are shown in Table I. For a bacterium, as shown in Fig. 14, the largest difference from the all-forces calculation occurs with Stokes drag–gravity case. The net X displacement of the bacteria is $\Delta X_p = \{9.971; 9.96; 9.94\}$ for (a), (b), and (c), respectively. For

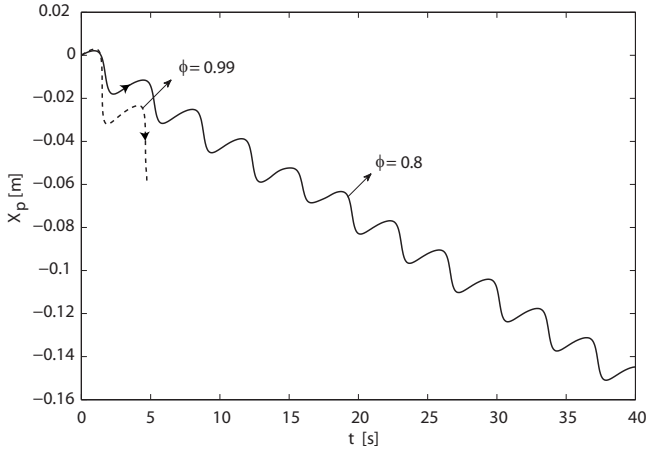

FIG. 13. Particle longitudinal path for bacteria with $Q=0$ and gravity in positive X direction. Fluid and particle parameters $\{\epsilon=0.0654; \mathrm{Re}=84.27; \alpha=0.0004; S=1.16; \mathrm{St}=5.687\times10^{-8}\}$. Initial position (0,0.9) and zero initial velocity, integration to $T=10$. Solid line is $\phi=0.8$; dashed line is $\phi=0.99$. Plot is in dimensional units.

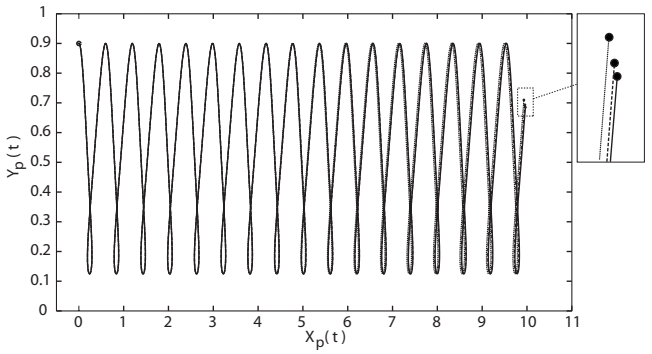

FIG. 14. Comparison of the effects of forces on particle motion for bacteria with $Q=Q_0$. Fluid and particle parameters $\{\epsilon=0.0654; \phi=0.8; \mathrm{Re}=84.27; \alpha=0.0004; S=1.16; \mathrm{St}=5.687\times10^{-8}\}$. Solid line is all forces; dashed line is Stokes drag, gravity, and Basset; dotted line is Stokes drag and gravity; integration carried to $T=20$. Gravity acts in the negative Y direction.

bacteria, considering the Stokes drag–gravity in (c) the underestimate in the net X displacement is around 0.3%, when compared to (a). A relatively larger percentage difference occurs for CaOx (see Fig. 15), again between all-forces case and the Stokes drag–gravity case. The net X displacement for CaOx is $\Delta X_p = \{17.787; 17.806; 17.858\}$. For CaOx, considering the Stokes drag–gravity case in (c), the overestimate in the net X displacement is around 0.4%, when compared to (a). Thus, for the ureteral peristalsis problem, if differences in the transit distance of less than 0.4% for 20 cycles are acceptable, only the Stokes drag and gravity and Basset forces need to be considered in the BBO equation.

Trajectory analysis gives us an insight into individual particle displacement. However, it does not provide information on the spatial distribution of particles as a group for which calculations of a group of particles should be made. For these computations only the Stokes drag, gravity, and Basset forces have been included. This approach inherently assumes that each particle within the group acts independently of the others and that the particle-fluid coupling is one way. An initial position for the dilute group of particles with zero initial

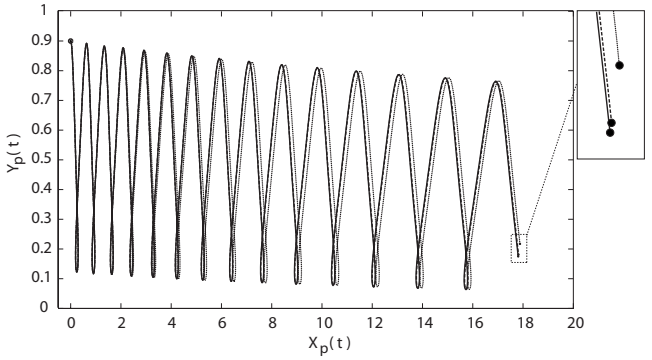

FIG. 15. Comparison of the effects of forces on the particle motion for CaOx with $Q=Q_0$. Fluid and particle parameters $\{\epsilon=0.0654; \phi=0.8; \mathrm{Re}=84.27; \alpha=0.0041; S=1.96; \mathrm{St}=9.997\times10^{-6}\}$. Solid line is all forces; dashed line is Stokes drag, gravity, and Basset; dotted line is Stokes drag and gravity; integration carried to $T=20$. Gravity acts in the negative Y direction.

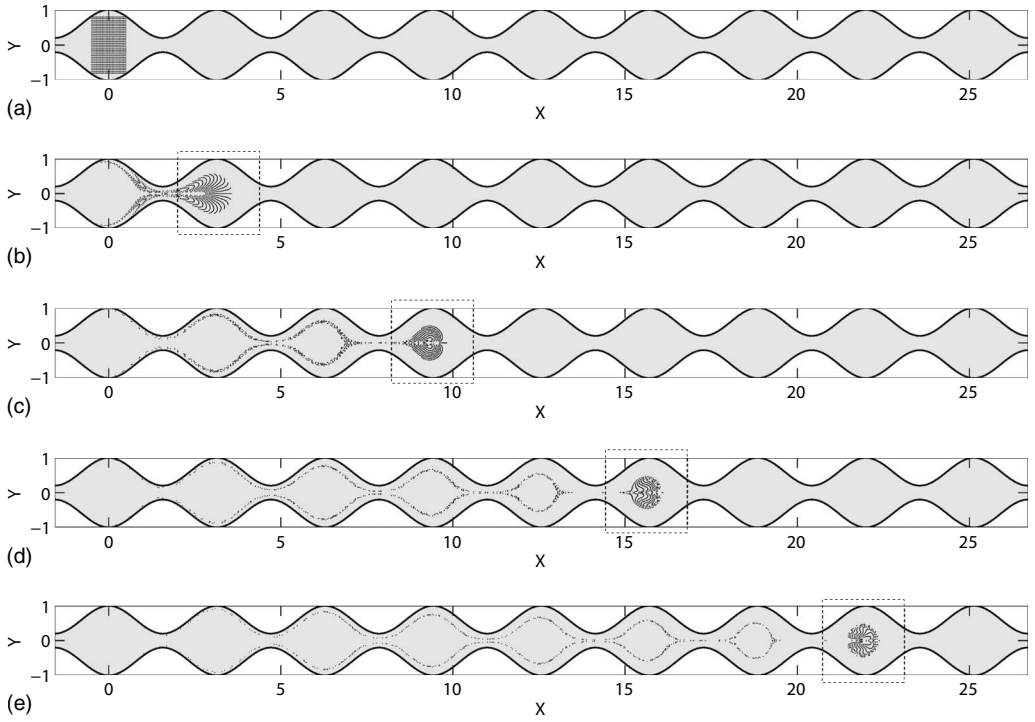

FIG. 16. (a) Initial, $T=0$, (b) $T=1$, (c) $T=3$, (d) $T=5$, (e) $T=7$. Position of 1280 bacteria particles initially evenly distributed within a rectangle defined by $X=\{-0.5,0.5\}$ and $Y=\{-0.8,0.8\}$. Fluid and particle parameters $\{\epsilon=0.0654;\phi=0.8;\mathrm{Re}=84.27;\alpha=0.0004;S=1.16;\mathrm{St}=5.68\times10^{-8}\}$. Gravity acts in the negative Y direction.

velocity is prescribed and then the positions of the particles are tracked in time. Figures 16 and 17 show the mixing of the dilute group of particles. The particles are initially distributed uniformly over a rectangle, the conditions of the fluid are those for ureteral peristalsis, and the dilute-suspension condition (interparticle spacing $\gtrsim 100d_p$) is maintained. Free pumping is examined for particles of both bacteria and CaOx.

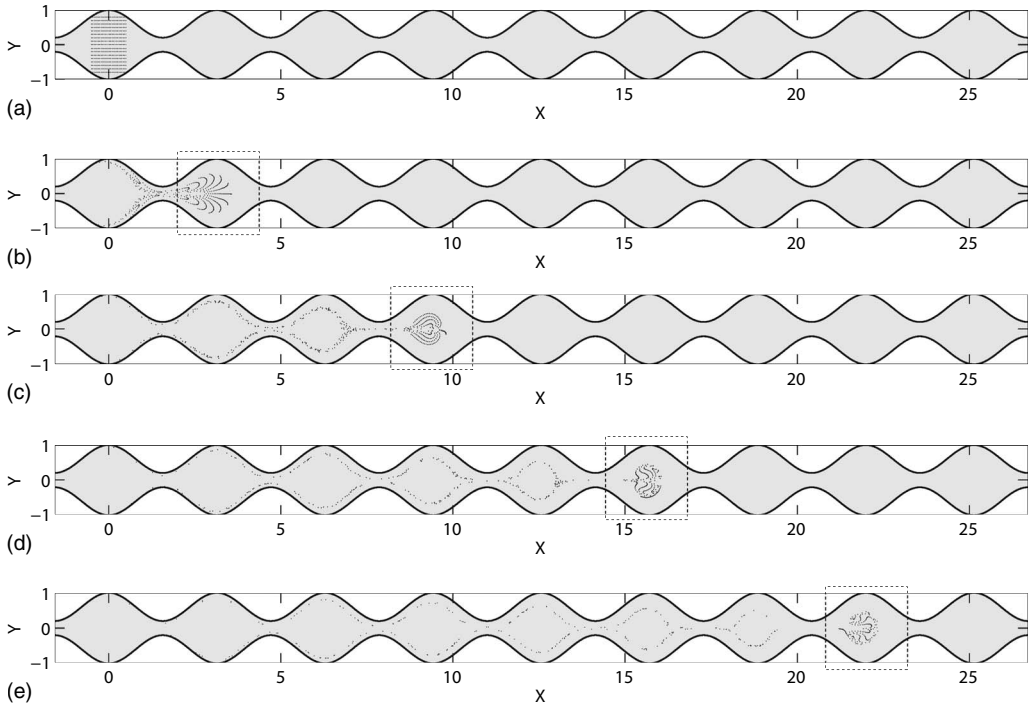

FIG. 17. (a) Initial, $T=0$, (b) $T=1$, (c) $T=3$, (d) $T=5$, (e) $T=7$.Position of 400 CaOx particles initially evenly distributed within a rectangle defined by $X=\{-0.5,0.5\}$ and $Y=\{-0.8,0.8\}$. Fluid and particle parameters $\{\epsilon=0.0654;\phi=0.8;\mathrm{Re}=84.27;\alpha=0.0041;S=1.96;\mathrm{St}=9.997\times10^{-6}\}$. Gravity acts in the negative Y direction.

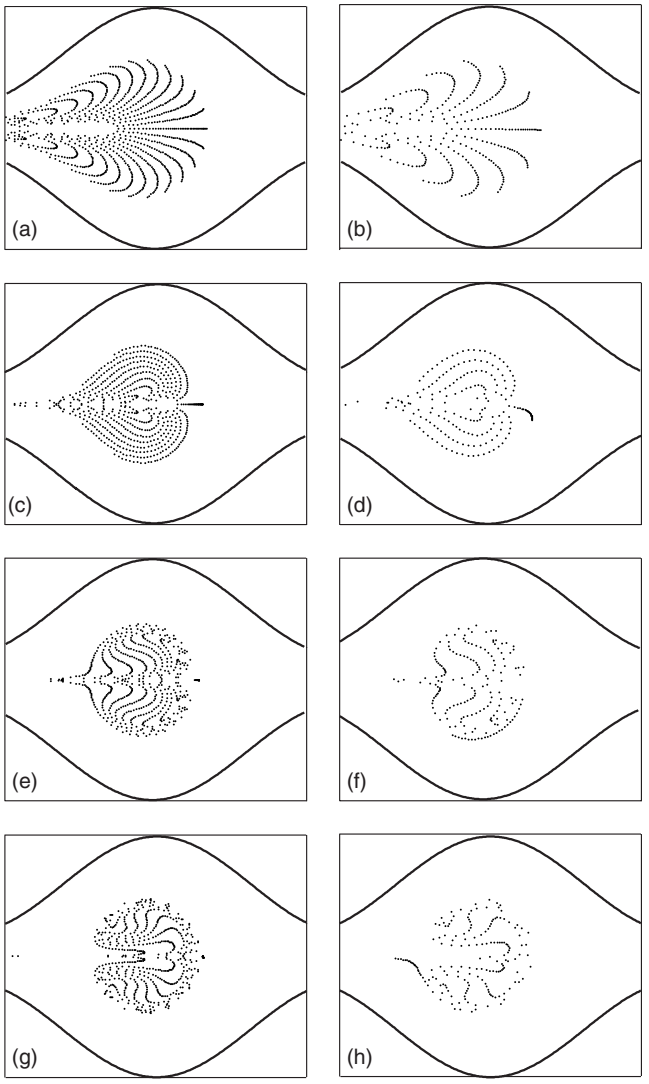

FIG. 18. (a) $T=1$ (bacteria), (b) $T=1$ (CaOx), (c) $T=3$ (bacteria), (d) $T=3$ (CaOx), (e) $T=5$ (bacteria), (f) $T=5$ (CaOx), (g) $T=7$ (bacteria), (h) $T=7$ (CaOx). Comparison of recirculations inside the bolus corresponding to Figs. 16 and 17.

Figure 16 shows the mixing and translation of a group of bacteria particles. Starting from their initial positions, particles near the center move forward and those near the wall are delayed. This creates a stellate appearance in the translation of the dilute group of particles. Note that some particles get closer to the wall and others participate in the formation of a bolus. After a while, the bolus completely detaches from the stellate. The process is similar for the CaOx particles, as shown in Fig. 17. Symmetry is broken because of stronger gravitational effects. A close-up view of the bolus is presented in Fig. 18; the recirculation inside the bolus is counterclockwise.

From this study of particle mixing, it is observed that particles tend to move to the wall (upper and lower). This is a possible explanation for the failure of particle clearing after ESWL. Particles in the bolus for CaOx can aggregate, leading to stone formation. For bacteria, particles near the wall can promote bacterial attachment to the inner mucosal tissue. Secondary effects of bacterial attachment include pathologies on the urinary tract such as ureteritis [50].

V. CONCLUSIONS

An analysis of two-dimensional peristaltic flow of a solid-liquid mixture in the ureter has been presented. Real parameters of ureteral peristalsis have been considered, but simplifications have been made with respect to two-dimensional geometry and sinusoidal wall form. The transport of small particles of finite mass is determined. The analysis provides insight into the mechanics of ureteral peristalsis in the presence of solid particles, as in ureteral lithiasis or bacterial transport. The influence of the fluid and peristalsis parameters on the flow was also examined. The pumping rate was nonlinear even for a relatively low Reynolds number. An asymptotic solution for the fluid flow up to second order in the wave number was obtained. Although the solution requires $\epsilon \ll 1$ and $\mathrm{Re}=O(1)$, based on experiments its validity can be extended to problems where the modified Reynolds number $\mathrm{Re}_m=\epsilon\,\mathrm{Re}\leq 10$, which corresponds to long wavelength and low frequency. Three flow situations result: backward, trapping, or augmented flow. When zero pumping is considered, reflux near the wall exists and particles are transported by the fluid. For a dilute group of particles starting at rest below the wave crest, some particles participate in the formation of a bolus and others approach the walls. Those approaching the wall can be trapped there, with possible pathological consequences.

ACKNOWLEDGMENT

J.J.-L. is grateful for support from the Mexican National Council for Science and Technology (CONACyT).

APPENDIX A: CONSTANTS

In Eq. (18), a_1-a_5 are

$$a_1=\frac{h''}{14}(6h^4+21h^3q+24h^2q^2+9hq^3)-\frac{(h')^2}{35}(33h^3+132h^2q+162hq^2+63q^3),$$

$$a_2=-\frac{h''}{40}(33h^4+141h^3q+216h^2q^2+108hq^3)+\frac{(h')^2}{40}(81h^3+360h^2q+612hq^2+324q^3),$$

$$a_3=\frac{h''}{140}(59h^4+315h^3q+20h^2q^2+414hq^3)-\frac{(h')^2}{140}(177h^3+840h^2q+1740hq^2+1224q^3),$$

$$a_4=-\frac{h''}{280}(15h^4+111h^3q+264h^2q^2+252hq^3)+\frac{(h')^2}{280}(51h^3+264h^2q+684hq^2+684q^3),$$

$$a_5=-h''(12h^2+18hq)+(h')^2(36h+72q).$$

APPENDIX B: INTEGRALS

The I's in Eq. (28) are

$$I_n = \int_0^\lambda \frac{dx}{h^n},$$

$$I_{pn} = \int_0^\lambda \frac{h'}{h^n} dx,$$

$$I_{ppn} = \int_0^\lambda \frac{h''}{h^n} dx,$$

$$I_{2pn} = \int_0^\lambda \frac{(h')^2}{h^n} dx.$$

Note that prime symbol indicates derivatives with respect to x, and n is a power exponent (e.g., integrating I_2 and I_3 from 0 to π, $I_2 = \int_0^\pi dx/h^2$ and $I_3 = \int_0^\pi dx/h^3$).

[1] A. H. Shapiro, M. Y. Jaffrin, and S. L. Weinberg, J. Fluid Mech. **37**, 799 (1969).
[2] M. Y. Jaffrin and A. H. Shapiro, Annu. Rev. Fluid Mech. **3**, 13 (1971).
[3] Y. C. Fung and F. S, Yih, J. Appl. Mech. **35**, 669 (1968).
[4] T. F. Zien and S. Ostrach, J. Biomech. **3**, 63 (1970).
[5] M. J. Manton, J. Fluid Mech. **68**, 467 (1975).
[6] P. Lykoudis and R. Roos, J. Fluid Mech. **43**, 661 (1970).
[7] D. J. Griffiths, J. Biomech. Eng. **111**, 206 (1989).
[8] S. Takabatake, K. Ayukawa, and A. Mori, J. Fluid Mech. **193**, 267 (1988).
[9] Q. Xiao and M. Damodaran, Int. J. Comput. Fluid Dyn. **16**, 201 (2002).
[10] F. Yin and Y. Fung, J. Fluid Mech. **47**, 93 (1971).
[11] A. Ramachandra Rao and M. Mishra, Acta Mech. **168**, 35 (2004).
[12] C. Pozrikidis, J. Fluid Mech. **180**, 515 (1987).
[13] S. L. Weinberg, E. C. Eckstein, and A. H. Shapiro, J. Fluid Mech. **49**, 461 (1971).
[14] M. Graw and H. Engelhardt, Urol. Int. **41**, 1 (1986).
[15] T. K. Hung and T. D. Brown, J. Fluid Mech. **73**, 77 (1976).
[16] C. Kleinstreuer, *Two-Phase Flow: Theory and Applications* (Taylor & Francis, London, 2003).
[17] N. A. Patankar and D. D. Joseph, Int. J. Multiphase Flow **27**, 1659 (2001).
[18] D. Drew, Phys. Fluids **22**, 2081 (1979).
[19] M. Ishii and T. Hibiki, *Thermo-Fluid Dynamics of Two-Phase Flow* (Springer, New York, 2006).
[20] H. Enwald, E. Peirano, and A. E. Almstedt, Int. J. Multiphase Flow **22**, 21 (1996).
[21] M. C. Shen, K. C. Lin, and S. M. Shih, SIAM J. Math. Anal. **12**, 49 (1981).
[22] L. M. Srivastava and V. P. Srivastava, J. Biomech. Eng. **111**(2), 157 (1989).
[23] K. S. Mekheimer, E. F. El Shehawey, and A. M. Elaw, Int. J. Theor. Phys. **37**, 2895 (1998).
[24] J. Misra and K. Pandey, Comput. Math. Appl. **28**, 131 (1994).
[25] M. R. Maxey and J. J. Riley, Phys. Fluids **26**, 883 (1983).
[26] C. F. M. Coimbra and R. H. Rangel, J. Fluid Mech. **370**, 53 (1998).
[27] J. C. Misra, *Biomathematics: Modelling and Simulation* (World Scientific, Singapore, 2006).
[28] R. M. Weiss, F. J. Tamarkin, and M. A. Wheeler, J. Smooth Muscle Res. **42**, 103 (2006).
[29] A. M. Siddiqui and W. H. Schwarz, J. Non-Newtonian Fluid Mech. **53**, 257 (1994).
[30] C. Crowe, M. Sommerfeld, and Y. Tsuji, *Multiphase Flows with Droplets and Particles* (CRC, Cleveland, 1998).
[31] W. Hinds, *Aerosol Technology: Properties, Behavior, and Measurement of Airborne Particles* (Wiley Interscience, New York, NY, 1999).
[32] S. L. Weinberg, Ph.D. thesis, MIT, 1970.
[33] S. Boyarski, C. Gottschalk, E. Tanagho, and P. Zimskind, *Urodynamics: Hydrodynamics of the Ureter and Renal Pelvis* (Academic, New York, 1971).
[34] M. S. Parmar, BMJ **328**, 1420 (2004).
[35] F. L. Coe, J. H. Parks, and J. R. Asplin, N. Engl. J. Med. **327**, 1141 (1992).
[36] M. Shigeta, Y. Kasaoka, H. Yasumoto, K. Inoue, T. Usui, M. Hayashi, and S. Tazuma, Int. J. Urol. **6**, 169 (1999).
[37] A. Costa-Bauzá, J. Perelló, B. Isern, and F. Grases, Urol. Res. **33**, 51 (2005).
[38] A. Guerra, F. Allegri, T. Meschi, G. Adorni, B. Prati, A. Nouvenne, A. Novarini, U. Maggiore, E. Fiaccadori, and L. Borghi, Clin. Chem. Lab. Med. **43**, 585 (2005).
[39] R. C. Walton, J. P. Kavanagh, and B. R. Heywood, J. Struct. Biol. **143**, 14 (2003).
[40] S. L. Weinberg, Invest. Urol. **12**, 255 (1975).
[41] A. H. Shapiro, Proceedings of Workshop on Ureteral Reflux in Children (National Academy of Sciences, Washington, DC, 1967), Vol. 1, pp. 109–126.
[42] F. Ramirez-Sejias, R. Gugig, A. Cepero-Akselrad, and A. Paredes, International Pediatrics **14**(2), 94 (1999).
[43] A. J. Wein, L. R. Kavoussi, A. C. Novick, A. W. Partin, and C. A. Peters, *Campbell-Walsh Urology* (Saunders, Philadelphia, 2007).
[44] H. N. Schulz and B. B. Jørgensen, Annu. Rev. Microbiol. **55**, 105 (2001).
[45] M. Godin, A. K. Bryan, and T. P. Burg, Appl. Phys. Lett. **91**, 123121 (2007).
[46] W. Höllander and S. K. Zaripov, Int. J. Multiphase Flow **31**, 53 (2005).
[47] H. C. Berg, *E. coli in Motion* (Springer, New York, 2003).
[48] A. H. Shapiro and M. Y. Jaffrin, J. Appl. Mech. **38**, 1060 (1971).
[49] S. A. Biondi, J. A. Quinn, and H. Goldfine, AIChE J. **44**, 1923 (1998).
[50] P. de Man, U. Jodal, K. Lincoln, and C. S. Edén, J. Infect. Dis. **158**, 29 (1988).